TUGA
MAPNA GROUP

Technical Review

MAPNA TURBINE ENGINEERING & MANUFACTURING CO. (TUGA)

Willpower to Empower Generations

No.10 - October 2018

TEN

Cover Page:

MAPNA Turbine Works, Karaj, Spring 2018

Photo by: Maadani, Behrooz

Editorial

Dear Colleagues, Partners and Professionals,

MAPNA Turbine have always sought to apply more advanced technological know-how and streamline the design and manufacturing process for its products by maintaining their technological agility, along with robustness and responsiveness towards dealing with the ever-increasing demands of today's energy industry. A brief account of a few recent achievements and technological breakthroughs is presented to you, our valued readers, in this edition of MAPNA Turbine Technical Review.

Design of a compressor impeller test bench as a fundamental step toward perfection in centrifugal compressors design is laid out in the first article. It facilitates and expedites the design process of tailor-made centrifugal compressors by making it possible to acquire practical performance data such as pressure, temperature and volumetric flow rate at each compressor stage.

The second article delineates successful integration and deployment of an advanced welding technology in fabrication process of two major MGT-70 components. In doing so, advantage is taken of numerous benefits it has on offer, and the outstanding preliminary results pave the way for more potential applications down the track.

The third essay is a design review of an entire exhaust system comprising diverter box and damper, guillotine damper, stack and silencers as well as supporting structure for a brand new MGT-80 heavy duty gas turbine. Advanced methodologies have been used to ensure an optimized design meeting all functional and structural requirements as well as environmental and safety regulations.

The fourth article is a success story of exploiting electron beam welding technology in welding low-pressure turbine shaft segments of the MGT-30 gas turbine, following in-depth scrutiny of welding parameters and test measurements. The technology provides exceptional welding characteristics rarely attainable through other conventional welding methods for turbine shaft segments made of typically hard-to-weld martensitic stainless steels.

The fifth and last article introduces an outstanding high velocity oxy-fuel sprayed nano-structure hardface coating developed to increase service lifetime of MGT-70 gas turbine compressor and MST-50C steam turbine blades. It withstands water droplet erosion typically observed on first few stages of gas turbine compressor, with wet compression system in service; or steam turbine blades at last stages. According to the comprehensive tests carried out, the developed coating system also demonstrates satisfactory corrosion resistance properties under both moderate and harsh corrosive conditions.

Please join us in relishing the detailed account of these subjects, in this issue of the Technical Review.

Respectfully,

Mohammad Owliya, PhD
Deputy General Director

MAPNA Turbine Company (TUGA)

October 2018

Table of Contents

1

Design of A Compressor Impeller Test Bench; A Significant Milestone in Designing Centrifugal Compressors

Introduction

Designing centrifugal compressors is an expensive, time consuming procedure which has convinced the manufacturers to pre-design main compressor components in a modular approach, and use them in new compressors. As we know, impellers are one of the most important components of a centrifugal compressor that transfers kinetic energy to the flow and results in velocity and pressure increase of the operating fluid. Impellers are pre-designed and sorted out in groups called "Impeller Families" and then according to the requirements of individual projects, including the intended flow rate and pressure ratio, one impeller family will be selected for the new compressor design.

In the design procedure of the impeller and following the implementation of 1D and 2D analyses, the prime geometry of the impeller is designed and then finalized and optimized (if required) through using computational fluid dynamics (CFD) tools. In order to validate the numerical results and to ascertain efficient operation of the designed impeller, it is required to perform an experimental run.

Taking advantage of the MAPNA Turbine's centrifugal compressor impeller test bench it will be made possible to requisition all compressor performance data such as pressure, temperature and volumetric flow rate at the end of each compressor stage consisting of the impeller, diffuser, U-bend and return channel. Furthermore, the polytrophic efficiency and work coefficient of each stage with regard to the impellers flow coefficient can be calculated. Fig. 1 represents sample performance curves of a typical compressor stage reported in the literature.

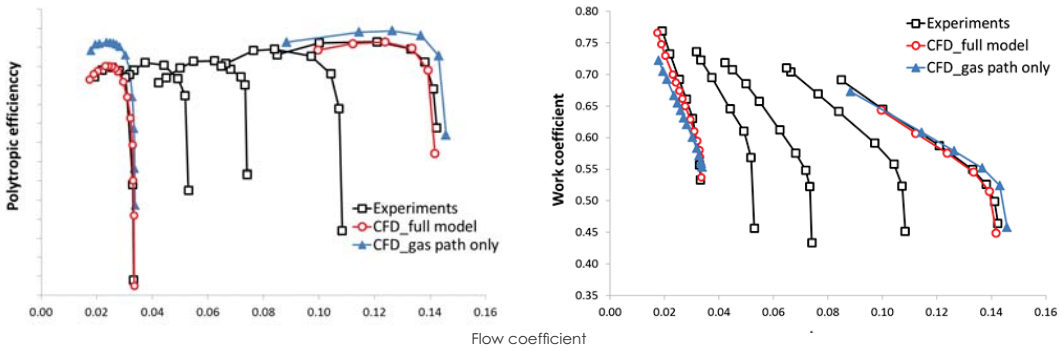

Fig. 1 - Typical experimental and numerical stage performance curves (courtesy of PCA Engineers)

As mentioned earlier, experimental runs are the only viable solution to analyzing the exact performance of the designed compressors. The compressor design process is also more accurate, when adequate reliable impeller performance data is provided. Hence the impellers belonging to the same family have similar performance specifications and taking advantage of the scaling method, one stage of the compressor is generally modeled, manufactured and tested, respectively. The overall performance of the impeller and compressor, the flow field inside the diffuser and the forces applied on the rotor will be investigated in more detail on smaller scales of the impeller models at the centrifugal compressor impeller test bench.

Impeller Family

Compressor manufacturers make no effort in reinventing the wheel by going all the way through the design process from scratch, for each single contract; instead they utilize a system of pre-engineered impellers and stages that have a more or less standardized geometry. At least the impeller blade shapes with inlet and outlet angles are fixed and scalable with other dimensions such as inlet and outlet width, eye and hub diameter for different applications. So, components with known characteristics are selected for each special case rather than designed anew. The overall compressor performance curve is also specified by aerodynamically superimposing the known stage curves. Scaling also allows adaptation to the conditions of the contract in question on the basis of limited deviations from the laws of aerodynamic similarity theories. The diversity and complexity in the realm of process compressor design is generally addressed by using the same elements with as few modifications as possible for all applications. A typical impeller family is shown in Fig. 2, for a complete range of flow coefficients [1].

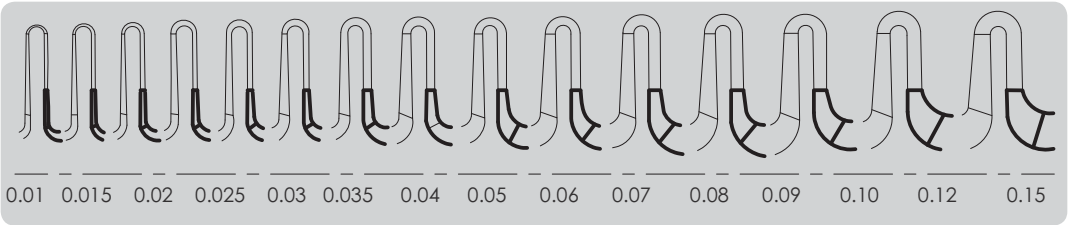

Fig. 2 - Typical impeller family [1]

Principles of Similarity for Compressible Flow Machines

According to the dimensional analysis [2], presented dimensionless groups are of critical importance when investigating the performance characteristics of compressors:

$$\frac{p_{01}}{p_{02}}, \frac{P}{\rho_{01} N^3 D^5}, \eta = f\left(\frac{s}{l}, \frac{h}{l}, \frac{\dot{m}}{\rho_{01} N D^3}, \frac{\rho_{01} N D^2}{\mu}, \frac{ND}{a_{01}}, \gamma\right)$$

In this equation, $\frac{ND}{a_{01}}$, $\frac{\rho_{01} ND^2}{\mu}$, $\frac{\dot{m}}{\rho_{01} ND^3}$, $\frac{P}{\rho_{01} N^3 D^5}$ and $\frac{p_{01}}{p_{02}}$ are dimensionless speed parameter, Reynolds number, dimensionless mass flow parameter, power coefficient and pressure ratio, respectively.

Impeller Scaling, Power and Rotational Speed Calculations

In order to extract the specifications of test bench electromotor, dimensional and performance analyses are conducted as described further at this section. Based on the dimensional analysis, dimensionless speed parameter and power coefficient shall be equal in the model and the prototype. Hence the rotational speed and power consumption of the model are calculated.

$$\frac{N_m D_m}{\sqrt{\gamma_m Z_m R_m T_{01m}}} = \frac{N_p D_p}{\sqrt{\gamma_p Z_p R_p T_{01p}}}$$

$$\frac{P_m}{\rho_{01m} N_m^3 D_m^5} = \frac{P_p}{\rho_{01p} N_p^3 D_p^5}$$

For example, for the prototype impeller specified in table 1, the rotational speed and power consumption are calculated as follows:

N_m = 9970 rpm

P_m = 8.27 kW

Table 1 – Prototype and model impeller specifications

Parameter	Prototype	Model
D(mm)	300	775
γ	1.403	1.353
Z	1	0.906
R(J/kg.K)	287.1	468.95
T(K)	298.15	317.15

Impeller Test Bench Mechanical and Electrical Components Overview

MAPNA Turbine's in-house centrifugal compressor impeller test bench is a modular facility capable of testing different impellers just by changing several components related to the impeller. Fig. 3 illustrates a longitudinal view of the impeller test bench. The driver of the test bench is a 75 kW variable speed electromotor. Power transmission is achieved by specially designed speed increasing flat belt-pulley rotating the main shaft by up to 13800 rpm. This kind of transmission system is advantageous due to its low price and simplicity. The test bench contains the axial inlet, inlet guide vanes (IGVs), impeller, diffuser, U bend, return channel and radial outlet. In order to measure required data for calculating the performance of the impeller, temperature and pressure sensors are installed at the inlet and outlet of the compressor and the flow rate is measured by an orifice installed within the upstream piping. It is to be mentioned that the minimum length of compressor inlet and outlet pipes as well as the location of all sensors are specified according to the guidelines of the ASME PTC 10.

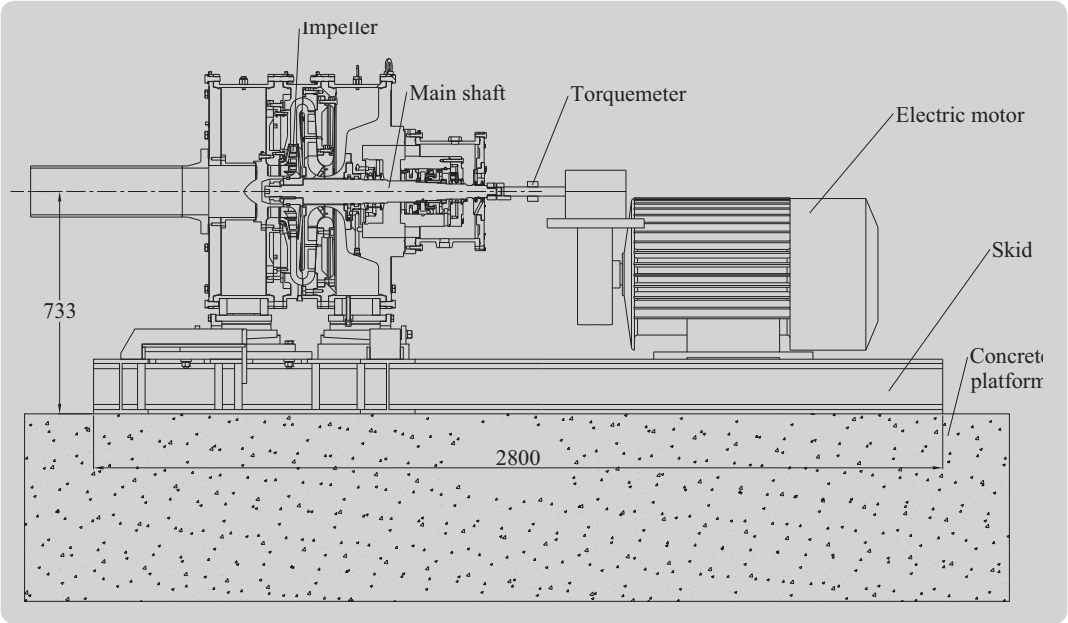

Fig. 3 – Impeller test bench, longitudinal view

The main specifications of the centrifugal compressor impeller test bench are presented in table 2.

Table 2 – Impeller test bench specifications

Parameter	Value
Maximum Impeller Speed	13800 rpm
Electromotor Power	75 Kw
Maximum Flow Rate	1.3 kg/s
Maximum Impeller Diameter	320 mm
Overall Dimensions (Length×Width×Height)	3800×3700×1500mm

A layout drawing of the impeller test bench including inlet and outlet pipes, inlet orifice and the pressure regulating valves, is depicted in Fig. 4.

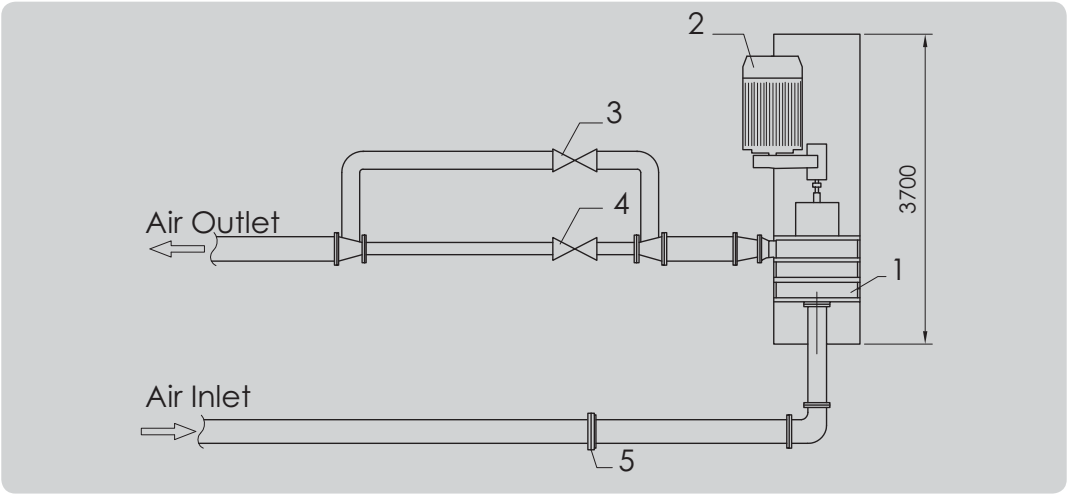

Fig. 4 – Layout drawing of the impeller test bench
(1- Compressor; 2- Electromotor; 3- Manual control valve; 4- Motorized control valve; 5- Orifice)

An absolute vibration sensor is installed on the casing to measure the vibration of the test bench. Appropriate temperature sensors are also used to measure the temperature of the journal and thrust bearings, meanwhile, a pressure sensor is installed on the thrust bearing to monitor the oil pressure within the bearing. Fig. 5 represents a P&I diagram of the impeller test bench. A complete list of items identified in the P&I diagram, is also presented in table 3.

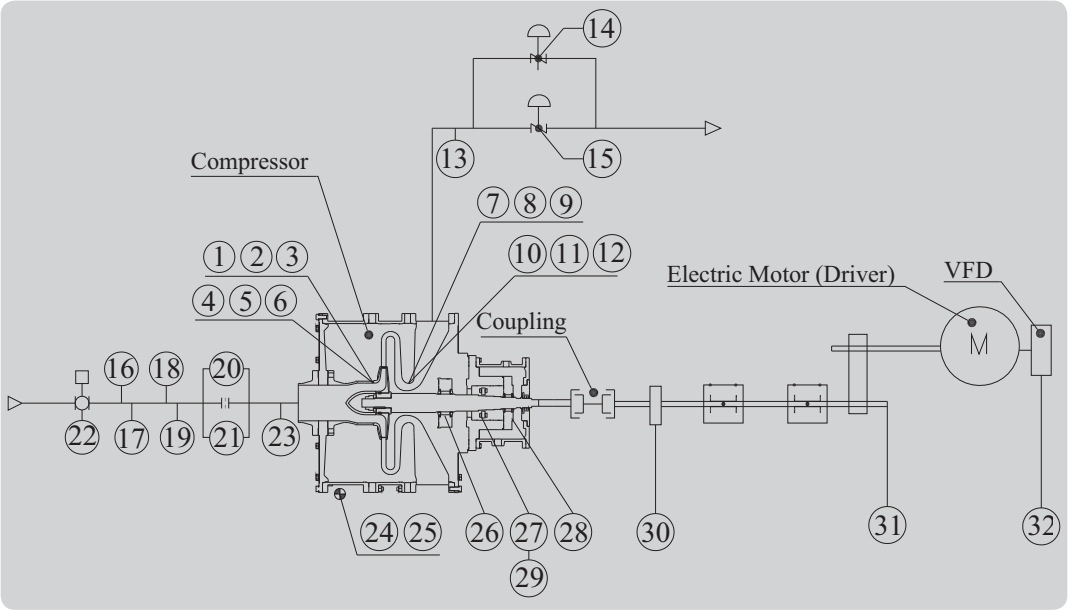

Fig. 5 – P&I diagram of the centrifugal compressor impeller test bench

Table 3 – Impeller test bench parts list

Pos. No.	Instrument
1-3; 7-9; 16; 17; 26-28	Temperature Sensor (RTD)
4-6; 10-12; 18; 19; 29	Pressure Transmitter
13; 23	Pressure Gauge
14	Manual Control Valve
15	Motorized Control Valve
20; 21	Pressure Differential Transmitter
22	Shut-off Valve
24; 25	Absolute Vibration Sensor
30	Torque-meter
31	Axial Relative Vibration Sensor
32	Speed Element

The centrifugal compressor impeller test bench is equipped with control and data logging systems containing several analogue and digital inputs/outputs. The control system controls the electro-motor speed and protects the system from any system components' malfunctions. In the meantime, this system records all instrument data such as flow temperatures and pressures. Data logging system records all data in desired logging rates and monitors all data online. The logged data will then be used for further analysis.

The installation positions of the temperature and pressure sensors marked with letters A and B are shown schematically in Fig. 6 at a typical compressor stage inlet and outlet, respectively.

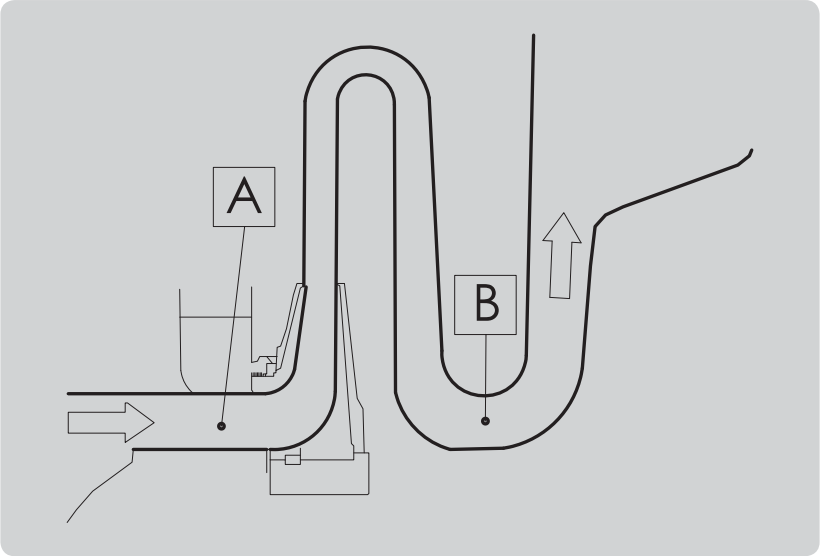

Fig. 6 – Installation positions of the temperature (A) and pressure (B) sensors at a typical compressor stage inlet and outlet

It is to be noted that, there are three temperature as well as three static pressure probes installed at each of the installation points shown in Fig. 6.

Concluding Remarks

MAPNA Turbine's centrifugal compressor impeller test bench was designed to facilitate and shorten the process of designing centrifugal compressors. Utilizing the centrifugal compressor impeller test bench facilities makes it possible to create impeller families to be used in centrifugal compressor design with desired process conditions.

It also makes it possible to evaluate performance of compressor impellers with different geometries without significantly altering the structure of the machine. In doing so, appropriate instruments to record flow data during the compression process, in addition to a proper control system to help log data, and to serve control and protection purposes are also incorporated into the system. Auxiliary equipment such as lubrication system as well as power and vibration measuring devices, required for safe and proper operation of the system are also appropriately designed and selected.

References

[1] K. H. Ludtke (2010); '*Process Centrifugal Compressors: Basic, Function, Operation, Design, Application*', Springer, Berlin, Germany.

[2] S. M. Yahya (2005); '*Turbines, Compressors and Fans*' (2nd edition), McGraw Hill, New York, NY, USA.

2

Productivity Upswing Using a Novel Technology in Weldings on Two Major Gas Turbine Components

Introduction

Keyhole-Tungsten Inert Gas (K-TIG™)[1] welding is an automated, full penetration process which operates at higher currents than conventional methods and pierces all the way through the joint, completing the weld in a fast, single pass process without a need for backing bar, edge preparation or filler materials. Thus, the resulting weld is an autogenous, 100% parent material without multiple fusion lines, disposed of any potential for inclusions, porosity and other defects typical of many multi-pass welding processes [1, 2].

A schematic representation of differences between conventional and keyhole TIG welding practices is shown in Fig. 1.

Fig. 1 - Conventional vs. K-TIG welding practices (courtesy of K-TIG, Australia)

[1] Keyhole TIG Limited (K-TIG) is an Australian company which has developed patented keyhole variant of GTAW (K-TIG) welding technology.

K-TIG welding process provides numerous benefits in terms of welding quality, productivity gains as well as energy, labour and cost savings for a wide range of applications and materials up to 16 mm in thickness [2].

A comparison between weld profiles and features of conventional TIG and K-TIG welds performed on 10.5 mm thick AISI 304 stainless steel plates is presented in Fig. 2.

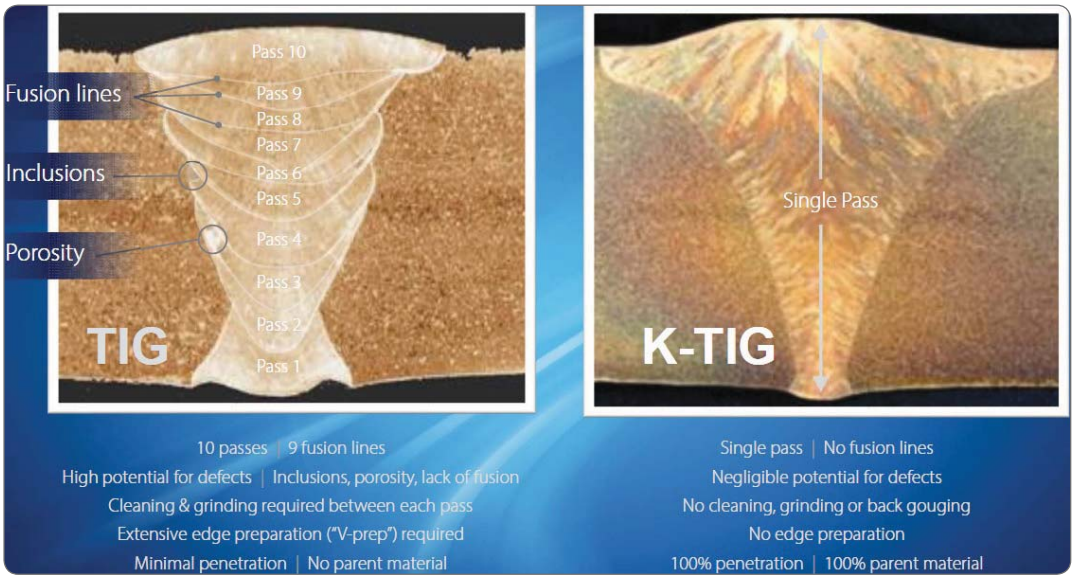

Fig. 2 Weld profiles and features of conventional TIG vs. K-TIG for 10.5 mm thick AISI 304 stainless steel (courtesy of K-TIG, Australia)

The main advantages of K-TIG welding process compared to TIG, MIG/MAG (Metal Inert Gas/Metal Active Gas) and PAW (Plasma Arc Welding) processes are as follows:

1. Fully automated process
2. No need for multi-pass welding
3. No need for highly skilled operators
4. Little or no need for costly consumables
5. Reduced power and gas consumption (Up to 95%)
6. Spared from extensive edge preparation processes
7. Tolerating more joint gap and Hi-Lo compared to PAW
8. Exceptional weld quality (Nuclear grade weld quality)
9. Higher welding speed than conventional TIG (Up to 100% faster)
10. No need for inter-pass and/ or post-weld back-gouging, finishing, cleaning and grinding

The promising prospects of K-TIG technology to increase productivity and welding speed while slashing the costs associated with conventional welding procedures led MAPNA Turbine to consider taking advantage of the numerous benefits K-TIG has to offer.

Materials and Methods

A K-TIG system was provided to carry out welding operations required for fabrication of two major MGT-70 gas turbine components: Mixing Chamber and Hot Gas Inner casing, at the first step. These elements are made of Nickel-based super alloys with a thickness of 10 and 12 mm, respectively. The following steps were planned to be taken:

1. Welding samples and setting the parameters
2. Performing required tests and analyzing the results
3. Preparing PWPS (Pre-Welding Procedure Specifications)
4. Welding all joints of hot gas inner casing at the final step
5. Welding a test coupon according to the PWPS developed
6. Welding individual mixing chamber plates together (longitudinal weld) prior to rolling
7. Welding mixing chamber joints (circumferential) at its final state (rolled & assembled)
8. Providing relevant Welding Procedure Specification (WPS) and Procedure Qualification Record (PQR)

The first six steps have been completely taken thus far and the last two steps will be taken in near future following fulfilment of some prerequisites.

In doing so and following some trial and error process, initial PWPS was prepared and a test coupon was welded. Welding conditions were as follows:

- Thickness: 10 mm
- Material: Inconel 617
- Welding Process: K-TIG
- Automation: Mechanized
- Welding Speed: 200 mm/sec

Laboratory Results

The welded test coupon was sent to Razi Metallurgical Research Center to undergo third-party in-depth tests and analyses. Qualification tests were performed according to the guidelines of the ISO 15614 international standard.

Laboratory report on the tests and analyses performed on a 10 mm thick Inconel 617 welded test coupon is presented below:

Visual inspection and macro-etch examination of the cross-section of the weld metal (WM) and heat affected zone (HAZ) shows:

- *Acceptable profile and convexity*
- *Complete fusion of root*
- *Thorough fusion between adjacent layers of WM, and between WM and BM*
- *No undercut was observed*
- *Root of weld is free from cracks when examined at a magnification of 25X*
- *Weld and HAZ are free from crack*
- *WM is free from porosity and other welding defects*
- *The leg of fillets are measured and are acceptable*

A macrograph of K-TIG welded test coupon cross-section, contained in the report is also shown in Fig. 3.

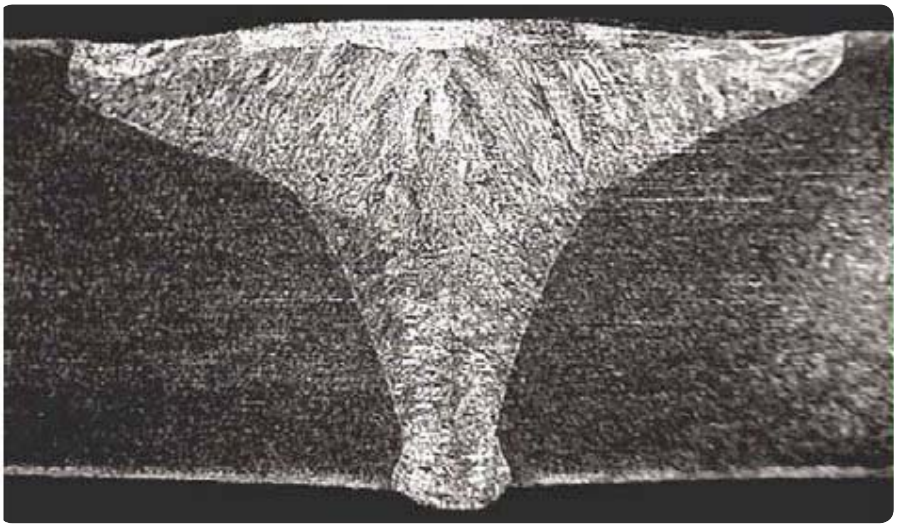

Fig. 3 – Macrograph of K-TIG weld in 10 mm thick Inconel 617 test plate

All mechanical test results were also satisfactory and the welded sample measured up well with all manufacturing specifications.

The individual mixing chamber plates were then welded together using K-TIG welding system, following preparation of the approved WPS and PQR. A schematic representation of the individual mixing chamber plates prior to them being K-TIG welded at the welding workshop along the longitudinal joints shown (dashed lines), is presented in Fig. 4. The implemented weld appeared well and the radiographic test results were also satisfactory.

In Fig. 5, a photograph of mixing chamber casing at its final rolled and assembled state is presented, illustrating circumferential joints to be welded using K-TIG technology at a later stage.

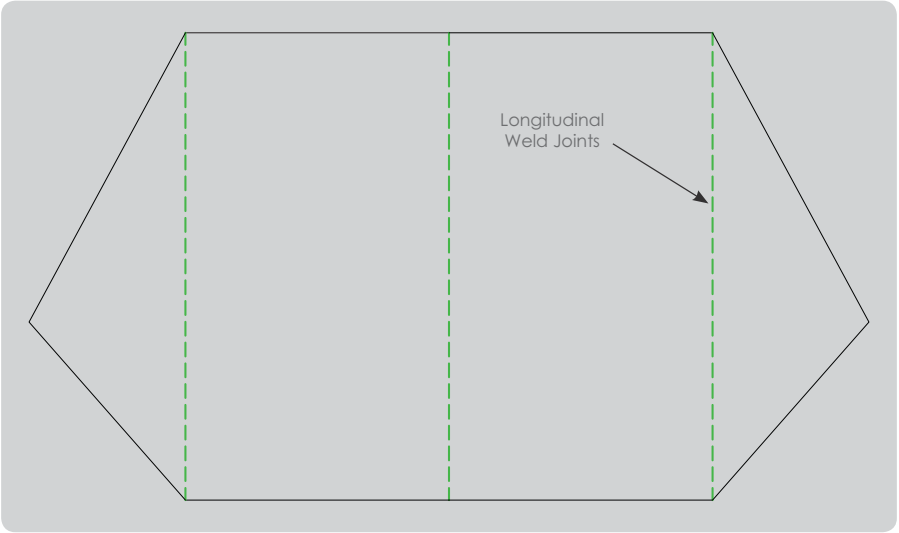

Fig. 4 – Mixing chamber plates longitudinal K-TIG welded joints prior to rolling (dashed lines)

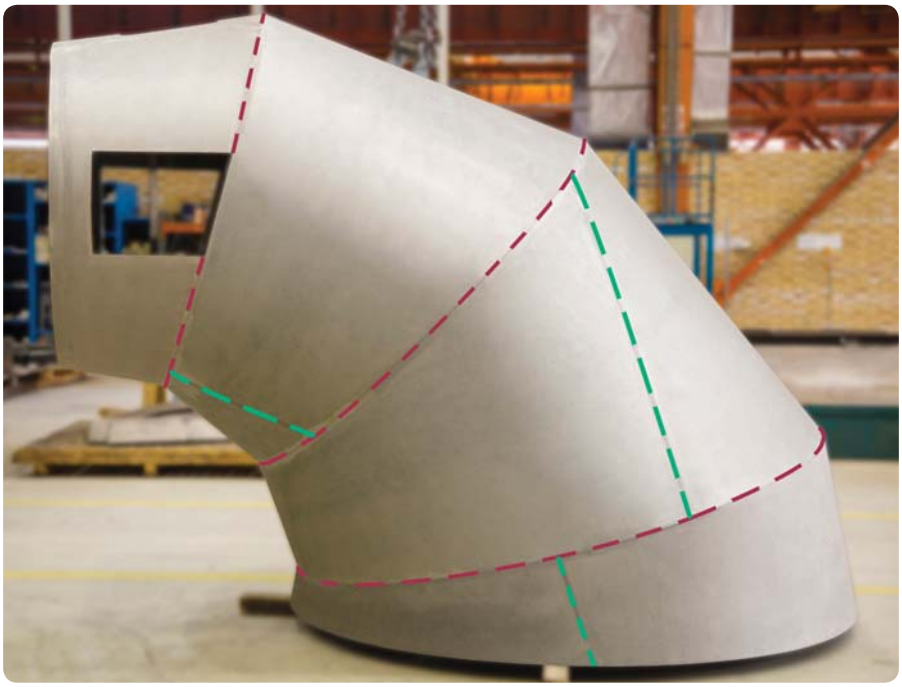

Fig. 5 – Mixing chamber casing longitudinal K-TIG welded joints (dashed green lines); circumferential joints to be welded at a later stage using K-TIG technology (dashed red lines)

For the first time using K-TIG welding system, production rate was more than 20 times greater than that of conventional Shielded Metal Arc Welding (SMAW) process with cost reductions due to the following reasons:

1. Significantly higher welding speed (approx. 200 mm/sec) than that of SMAW process
2. Single pass (full penetration) welding procedure
3. Square butt joint design and elimination of filler material
4. Not performing any back grinding and NDT tests thereafter
5. Not requiring joint preparation and any inter-pass cleaning and grinding

Prospects

K-TIG welding is considered a cost effective process for welding different parts and elements in a large diversity of industrial sectors. It provides substantial cost savings and productivity gains, making it a valuable tool with numerous applications in power generation industry where abundantly large amounts of welding are required. MAPNA Turbine has already begun to integrate and deploy advanced K-TIG welding technology with fabrication process of several major gas turbine components with outstanding preliminary results and much more potential applications in the future.

References

[1] 'What is K-TIG' (Online). Available at: www.k-tig.com/what-is-k-tig

[2] 'Benefits of K-TIG' (Online). Available at: www.k-tig.com/k-tig-benefits

3

MGT-80 Heavy Duty Gas Turbine Exhaust System; Design Review

Introduction

Exhaust system as one of the main heavy ancillary parts of a gas turbine, plays a critical role in single and combined cycle power plants. Gas turbine and Heat Recovery Steam Generator (HRSG) requirements as well as noise emission level and environmental concerns must be all fulfilled, while there are also complicated structural and mechanical aspects to be addressed.

MGT-80 exhaust system design comprising diverter damper, guillotine damper, stack and silencers as well as supporting structure is introduced in this article.

Background

Utilizing state-of-the-art technologies, the MGT-80 heavy-duty gas turbine offers outstandingly high nominal power output of 308 MW in simple cycle applications.

The machine is produced by MAPNA Turbine under a license agreement for SGT5-4000F with SIEMENS AG. However, design of intake and exhaust of the machine is by MAPNA Turbine, in accordance with SIEMENS technical specifications as well as customer requirements and local regulations.

A comparison of the performance data for the MGT-70 and MGT-80 heavy-duty gas turbines is presented in table 1. In order to meet the stringent requirements of the international environmental standards, the height of the MGT-80 exhaust system has increased up to 35 m, setting a new record for heavy-duty gas turbines within the country. Keeping the noise levels below the 85 dB was another challenge to overcome. This criterion was finally fulfilled through designing 28 silencer baffles with minimal pressure and gas velocity drops.

Table 1- MAPNA Turbine's heavy-duty gas turbines performance data

Gas Turbine Model	Power (MW)	Gas Flow (Kg/s)	Hot Gas Temperature (°C)
MGT-70(3)	185	554	544
MGT-80	308	724	581

A new method of mechanical and structural design as well as new standards were used to accomplish this project. Load and Resistance Factor Design (LRFD) method was used as a new way of optimal and safe structural design. Applying this code, full capacity of steel parts could be used during operation. Furthermore, designing such a huge structure for high risk earthquake zones would require more considerations for covering performance range and reliability of the equipment during and after seismic phenomena. Applying nonlinear structural analysis for standard and specific seismic spectrum, would guarantee safe performance of the exhaust system following an earthquake.

A Three-dimensional view of the designed MGT-80 gas turbine exhaust system model is presented in Fig. 1.

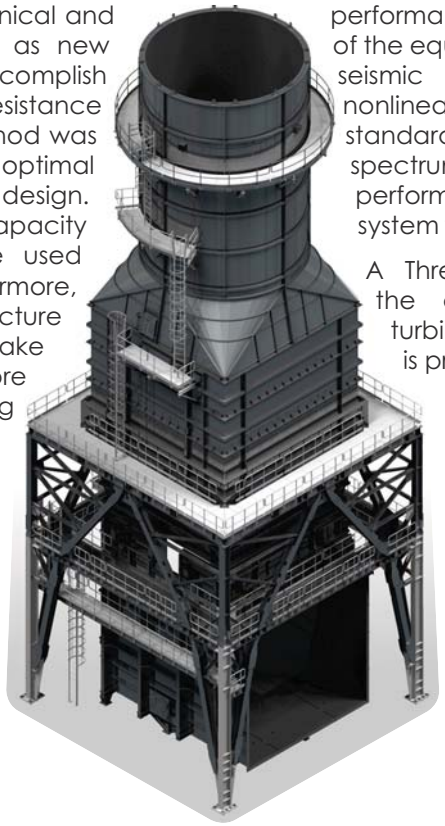

Fig. 1 – 3D view of the MGT-80 gas turbine exhaust system model

Design Phase

- **Flow Field Analysis**

Overall dimensions of the exhaust system were specified via analytical calculations. Complete 3D steady state turbulent flow analysis was carried out using computational fluid dynamics (CFD) software to investigate flow field and pressure drop through exhaust system from turbine outlet to the end of the stack, where gas is released to the atmosphere. The solution was achieved using a total of 39.5 million nodes in the meshed model of the exhaust fluid.

Obtaining the most accurate solution would require complete distribution of flow properties to be applied at the inlet boundary of the model. The velocity, temperature and pressure distributions at the inlet of the model are shown in Figs. 2(a) to 2(c), respectively.

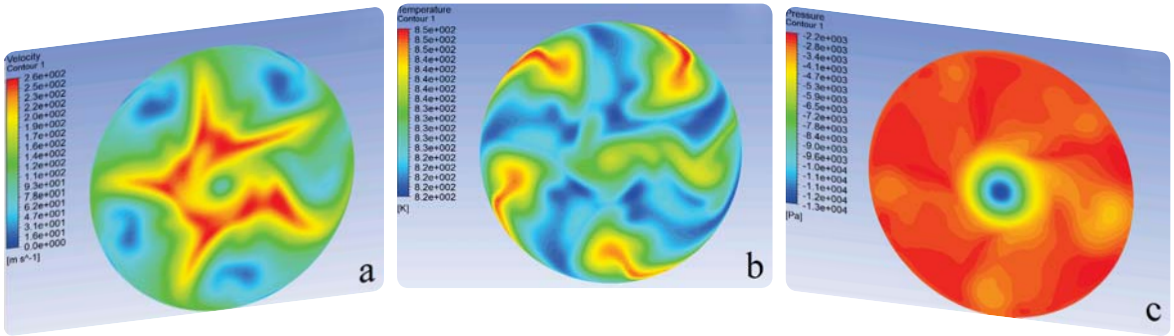

Fig. 2 – Velocity (a), Temperature (b) and Pressure (c) distribution contours at the inlet of the model

Interactions between the gas turbine and the exhaust system were investigated to optimize the pressure drop through the exhaust system. Subsequently, the final gas path and the exhaust geometry were finalized. Fig. 3 represents gas flow streamlines colored by velocity magnitude at simple cycle operation mode. Maximum area coverage and uniform gas flow distribution were achieved in the final design. Figs. 4(a) and 4(b) also show temperature and velocity distributions respectively at the mid-section of the exhaust system.

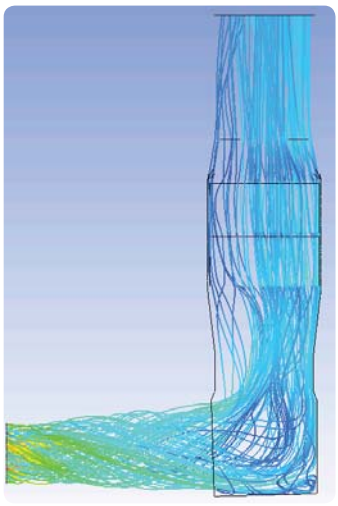

Fig. 3 – Exhaust gas flow streamlines

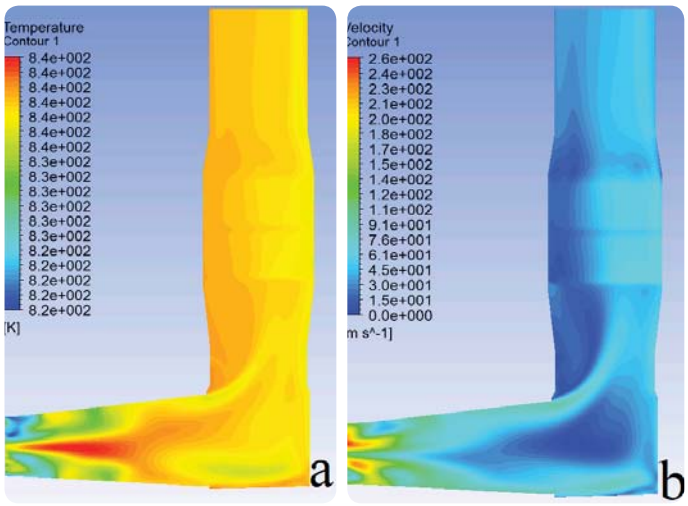

Fig. 4 – Temperature (a) and velocity (b) contours at the mid-section of the exhaust system model

In addition to the investigation and optimization of the pressure drop across the model, a survey on the forces applied on silencer baffles by the gas flow was also carried out.

Since lateral and vertical forces affect the design of silencer baffles, it was necessary to make sure that they were within the acceptable ranges. Proper distribution of gas flow within the baffles led to acceptable levels of forces at this section of the exhaust system model.

■ Structural Design

Structural design of the MGT-80 gas turbine exhaust system was carried out using finite element method and based on the seismic provisions of the ASCE and AISC standards. A 3D model of the designed diverter box is represented in Fig. 5. An integrated model of the stack and supporting structure is also shown in Fig. 6.

Fig. 5 – 3D model of the diverter box

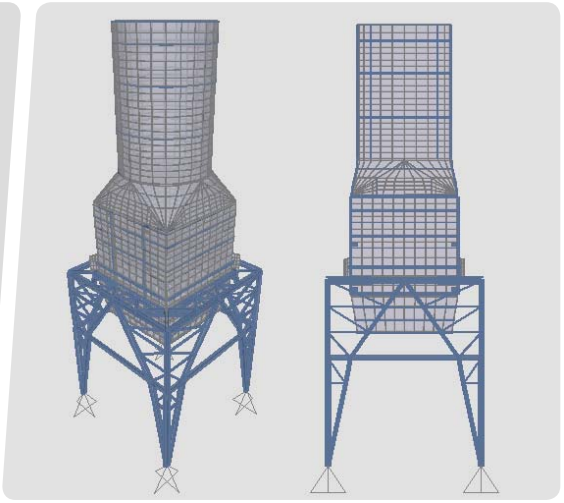

Fig. 6 – Integrated model of the stack and supporting structure

Using braced frame system to withstand lateral forces brings about minimal lateral deflection of the exhaust structure and the simplest and safest expansion joint between the diverter box and the stack, consequently.

Additional control for distribution of plastic hinges was carried out and time history method for important earthquake acceleration records was applied. Fig. 7 shows seismic records of "Northridge" scaled to PGA=0.35g for return period of 475 years. Additionally, response spectrum and modal analyses were used to control the structural behavior of the exhaust system during operation and earthquake. Fig. 8 shows deflection of the exhaust system and supporting structure during seismic record of "Northridge" at 4 different time steps.

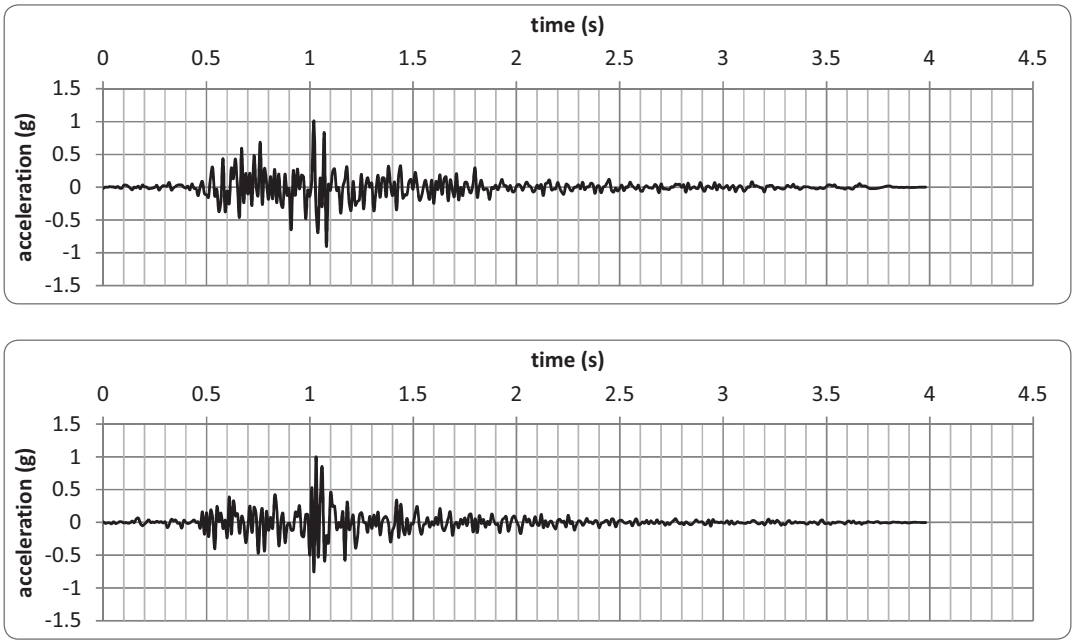

Fig. 7 – Northridge longitudinal (top) and orthogonal (bottom) seismic records

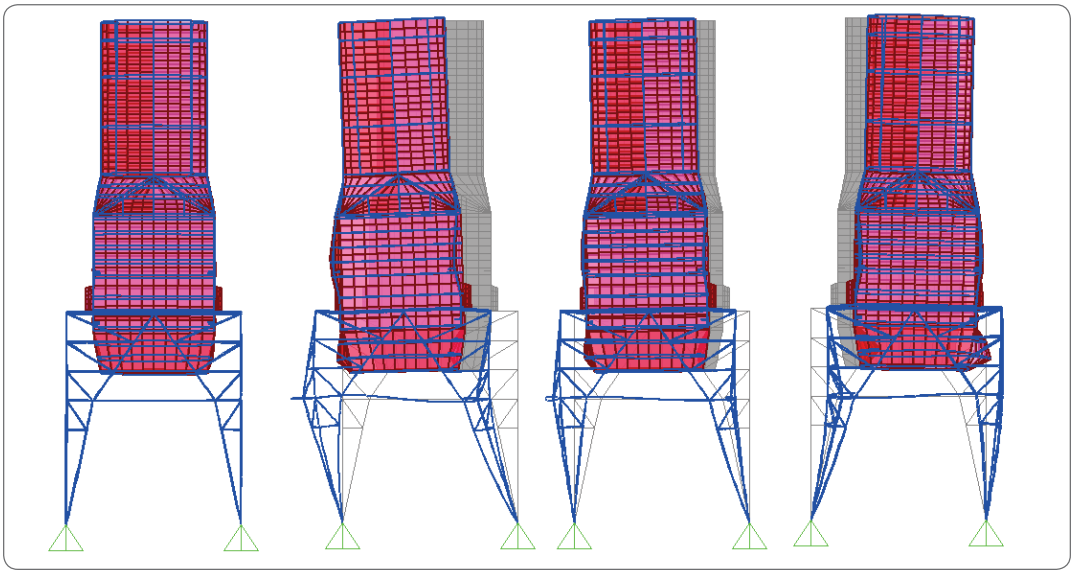

Fig. 8 – Deformation shape of bypass stack and supporting structure during seismic record

Fig. 9 represents typical results of the structural analysis performed on the diverter box of the MGT-80 gas turbine exhaust system.

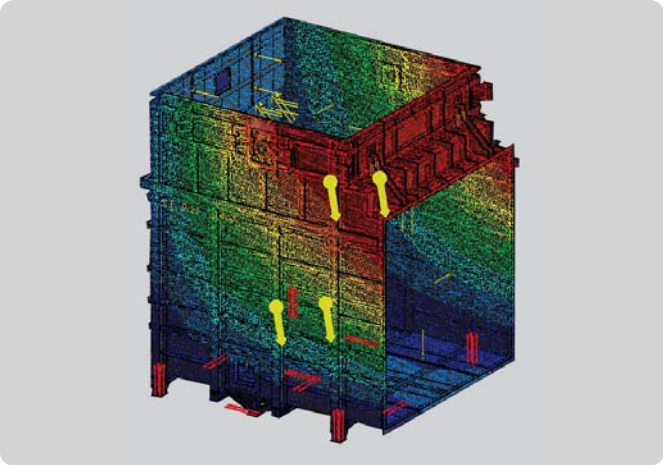

Fig. 9 – Sample results of the structural analysis performed on the diverter box (earthquake simulation)

Diverter and guillotine dampers were also modeled after determining the overall dimensions and specifications of these equipment items based on MGT-80 gas turbine requirements. In order to improve the design, fluid flow as well as thermal and structural analyses were performed on the model. The result led to one of the biggest diverter dampers in power plant projects with 6.9×6.9 m gas path area.

Fatigue, creep and vibrational analyses were also performed on the model due to presence of thermal effects. In detail design phase, the previous erection and operation experiences with other gas turbines exhaust systems were also taken advantage of.

■ Noise Control

To reduce the emitted noise from gas turbine exhaust into the environment, silencer elements were incorporated into the stack. The maximum allowable sound pressure level is defined by the client. The silencer is designed based on this value, sound power level of gas turbine exhaust, dimensional limitations and allowable pressure drop. Fig. 10 shows the effect of silencer in decreasing sound pressure level at receiver point. Red bars indicate sound pressure levels without silencer and green bars indicate the values with the silencer in place. The diagram shows further reduction in sound pressure levels especially in the range of 500 to 2000 HZ frequencies.

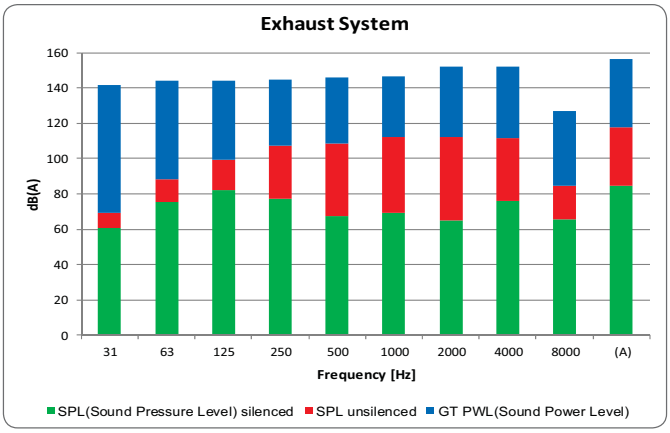

Fig. 10 – Effectiveness of silencer on stack noise reduction

Manufacturing

Domestic technologies available satisfy all design requirements for fabrication. A new diverter damper was manufactured and installed at Rudshur power plant southwest of Tehran.

To cover MAPNA Turbine's scope of supply for Hengam combined cycle power plant, south of Iran, an entire exhaust system including diverter box and damper, guillotine damper, bypass stack, hydraulic pressure unit, sealing air system as well as other related equipment will be supplied. Metal work on different parts of the exhaust system is carried out before shipment and the final assembly of parts will be performed on site.

Fig. 11 presents several photographs of different parts of the bypass stack and diverter box during manufacturing process.

Fig. 11 – MGT-80 gas turbine exhaust system manufacturing process in action

Concluding Remarks

A complete MGT-80 gas turbine exhaust system is manufactured and soon will be installed in Hengam combined cycle power plant, south of Iran. This product is the result of more than one year of engineering activities including noise calculations, structural and mechanical procedures, welding designs and electrical parts design, selection and implementation. This huge equipment is compatible with thermodynamic demands of gas turbine and HRSG system. All environmental and safety regulations were also observed during the basic and detail design processes in order to present an advanced and optimized product. Also, in order to minimize transportation issues, the exhaust system is divided into smaller parts which could be easily assembled on site. The final product is a 35 meter high exhaust with a diameter of 7000 mm. Below are some of the main features of the exhaust system specifically designed for MGT-80 heavy duty gas turbine:

- Low noise levels
- Easy to transport
- Easy and fast assembly at site
- Low hazard of pollution distribution
- Low risk of vibrations during operation
- Performance-based design for earthquake
- Optimal distribution of flow and low pressure drop
- Compatible with future versions of MGT-80 gas turbine

4

Electron Beam Welding of Martensitic Stainless Steel Turbine Shaft; Now a Practically Verified Option

Introduction

Stainless steels are widely used due to their excellent mechanical properties such as high strength, corrosion and fatigue resistance, etc, which makes them a perfect choice for critical applications. Martensitic grades are one of the least available stainless steel grades. It is quite a bit of a challenge to improve the strength and hardenability of the martensitic grades as they are associated with higher carbon contents in comparison with other stainless steel grades. Nitrogen is also sometimes added to further enhance the strength of these materials [1]. Martensitic stainless steel contains no or rather small amount of Nickel and Molybdenum is seldom added either. By adding some nickel and reducing the carbon content, the rather poor weldability of the martensitic stainless steel grades would be improved [2].

Martensitic stainless steels, as superior materials in rotary machine applications, are often hard to be welded due to their intrinsically high strength and hardenability which makes them brittle and prone to development of cold cracks especially in the Heat Affected Zone (HAZ). One of the main setbacks associated with martensitic stainless steels is that they regularly need to be preheated prior to welding [2]. Nevertheless, using Electron Beam Welding (EBW) as an extremely effective method of joining makes preheating unnecessary.

EBW is one of the commonly used welding practices for joining materials in high demand, in different industries. The primary advantage of EBW is its high depth-to-width ratio which results in a very strong weld. The quality of weld depends on several parameters such as accelerating voltage, beam current, welding speed, focus current and vacuum level.

EBW has a high power density which leads to small HAZ areas as well as high heating and cooling rates. EBW is a technology used to develop welded structures and components with characteristics rarely attainable through other conventional welding methods. The main advantages associated with this technique are deep and narrow defect-free welds, minimal thermal affected zones as well as a high joining rate [3]. EBW is a quite complex process whose result depends on a large number of parameters such as material characteristics and EBW machine properties. The main objective of this investigation was to ascertain the appropriate welding parameters thresholds to weld the Low-Pressure Turbine (LPT) shaft of the MGT-30 gas turbine, using EBW technology.

Methods

As the first step, a Russian stainless steel grade of 07X12HMБФ-Ш (ЭП609-Ш) sample was welded using EBW process. The chemical composition and mechanical properties of the base material along with the standard reference values are presented in tables 1 and 2, respectively.

Table 1 – Chemical composition of the 07X12HMБФ-Ш (ЭП609-Ш) grade stainless steel

Elements	%C	%Si	%Mn	%Cr	%Ni	%Mo	%Nb	%V	%S	%P	%Fe
Standard Values	0.05 0.09	< 0.6	< 0.6	10.5 12	1.4 1.8	0.35 0.5	0.05 0.15	0.15 0.25	< 0.02	< 0.03	Base
Measured Values	0.07	0.32	0.17	10.79	1.62	0.37	0.09	0.19	0.004	0.030	Base

Table 2 – Mechanical properties of the 07X12HMБФ-Ш (ЭП609-Ш) grade stainless steel

	Yield Strength (MPa) Min,	Tensile Strength (MPa) Min,	Elongation,% Min,	Reduction of Area,% Min,	Impact, J Min,
Standard Values	900	Min,	Elongation,%	55	69
Measured Values	901	Min,	Reduction of Area,%	66.5	88.2

Fig. 1 depicts the microstructure of the 07X12HMБФ-Ш (ЭП609-Ш) grade stainless steel. The fully tempered martensitic structure of the base material is completely obvious in this picture.

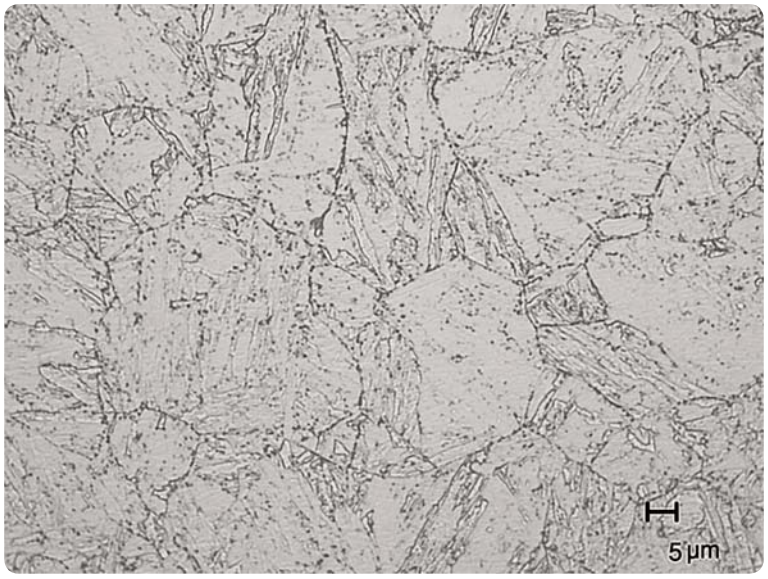

Fig. 1 – Microstructure of the 07X12HMБФ-Ш (ЭП609-Ш) grade stainless steel

Welding was performed using a high vacuum EBW machine with a chamber size of 1.5×1.5×4 m. Schematic representation of the MGT-30 gas turbine LPT shaft as well as outline and detail drawings of the butt-square welded joint to be formed are presented in Fig. 2.

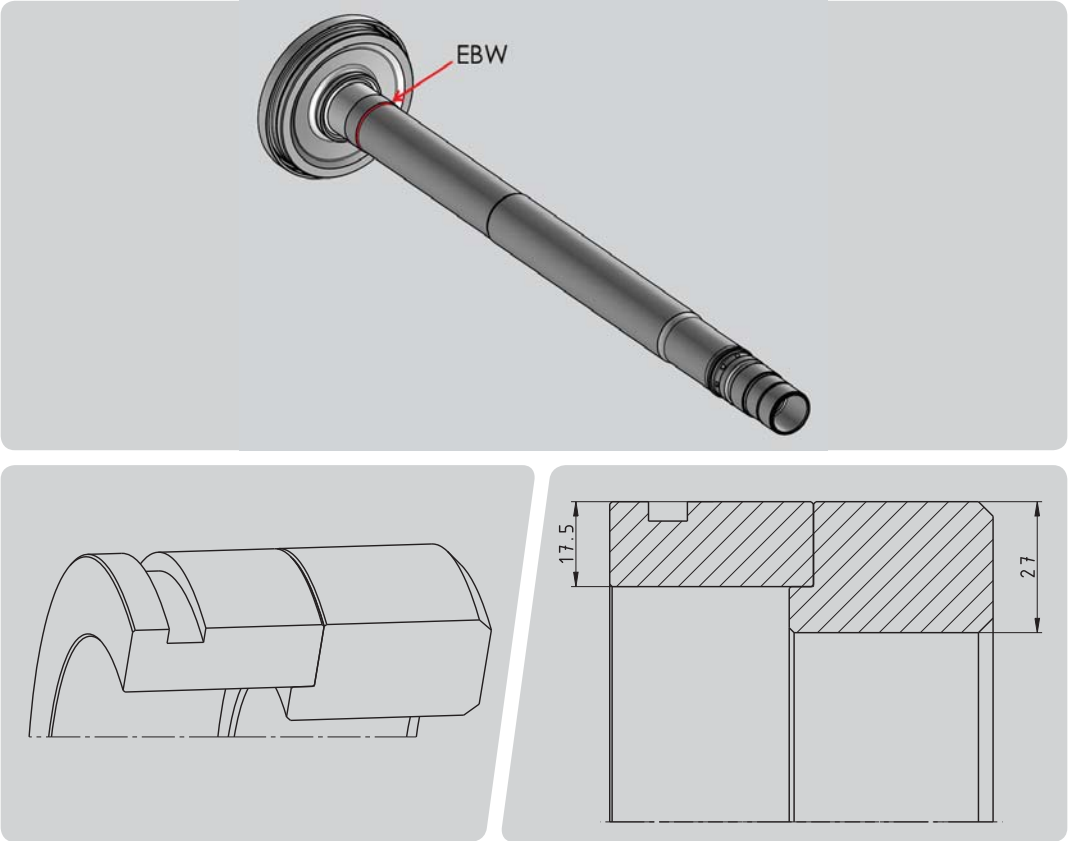

Fig. 2 – Schematic representation of the MGT-30 gas turbine LPT shaft (top), outline and detail drawings of the butt-square weld joint design (bottom)

Total thickness of the joint is 27 mm comprising of main and backing plates of 17.5 mm and 9.5 mm thick, respectively. The welding was performed autogenously without using any filler material.

Microstructural evaluation of the welds performed was carried out using an optical microscope. Samples taken were chemically etched using VILLELA solution prior to implementation of further analyses. Tensile tests were carried out according to the guidelines of the ASTM E8 international standard for sub-size specimen. The Charpy impact and bend tests were also conducted in accordance with the guidelines of the ISO 9016 and ISO 5173 international standards.

Welding Test Procedure

To establish optimum welding parameters for welding LPT shaft segments of the MGT-30 gas turbine, a 27 mm thick flat plate was welded without any weld seam via EBW machine using different parameters. Welding parameters including working distance and lens current are listed in table 3 for a single beam voltage. Welding was accomplished via different welding speeds i.e., slow, moderate and fast to reach a full-penetration joint. Full-penetration state was ensured once tiny splashes were observed at the root of the specimen.

Table 3 – Welding parameters used for welding of the flat plate using EBW machine

Speed Condition	Welding Speed (mm/min)	Voltage (kV)	Working Distance (mm)	Lens Current (mA)	Beam Current (mA)
Slow	200	60	336	400	100
Moderate	250	60	336	400	115
Fast	500	60	336	400	150

Fig. 3 shows macrostructure of the electron beam welds performed using specified welding speeds. It can be seen that although the weld and HAZ areas were likely to get narrower by increasing the welding speed, some defects were also introduced in the weld metal (as indicated in Fig. 3) due to higher welding speeds. This was probably because the melted metal hardly had enough time to solidify and fill the seam when the speed of welding was relatively high.

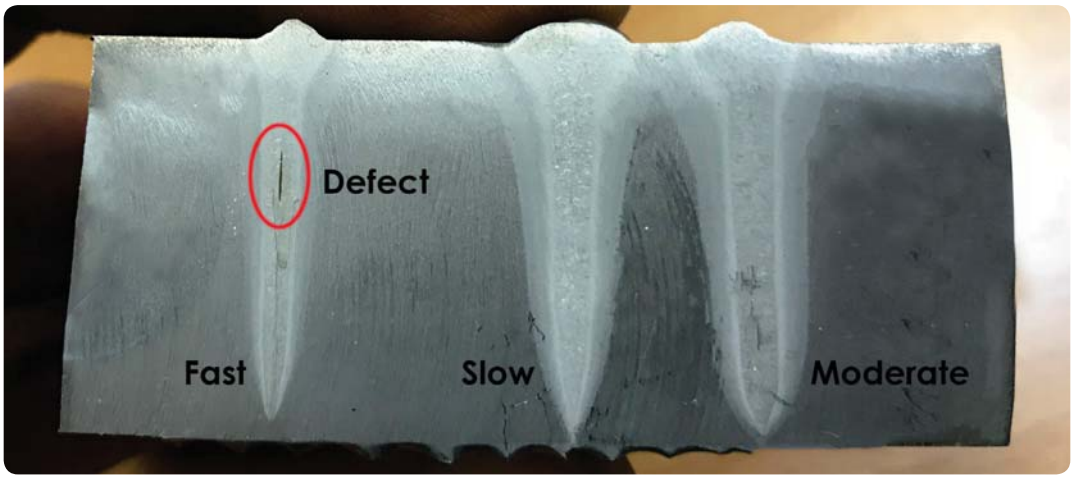

Fig. 3 – Macrostructure of the electron beam welds performed on a flat plate using different welding speeds

Thus, moderate welding speed was established as the optimum welding speed to avoid ending up with such defects.

To make up for the circular shape of the LPT shaft weld joint and to establish optimum welding parameters on such geometry, same test welds were carried out on a pipe sample of the same thickness, i.e., 27 mm, converting the established optimum linear welding speed to its matching rotational speed of the specimen, as shown in Fig. 4.

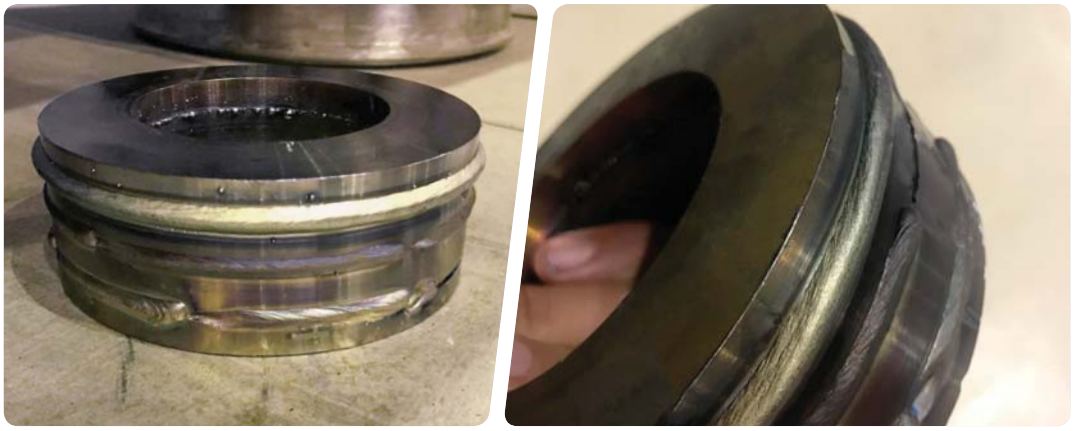

Fig. 4 – 07Х12НМБФ-Ш grade pipe sample welded using different beam currents

The parameters of the performed test welds as well as test observations are presented in table 4.

Table 4 – Welding parameters used for welding of the pipe sample using EBW machine

Rotational speed (deg/min)	Voltage (kV)	Working distance (mm)	Lenz current (mA)	Beam current (mA)	Test Observation
273	60	336	400	115	**Partial Penetration**
273	60	336	400	120	**Full Penetration**
273	60	336	400	125	**Excess Penetration**

Fig. 5 represents the cross-sections of the electron beam welds performed on 27 mm thick 07X12HMБФ-Ш pipe sample using different beam weld currents listed in table 4. As it can be seen in this figure, the optimum welding current for a full penetrant electron beam weld performed on pipe sample is 5 A more than that for the flat plate.

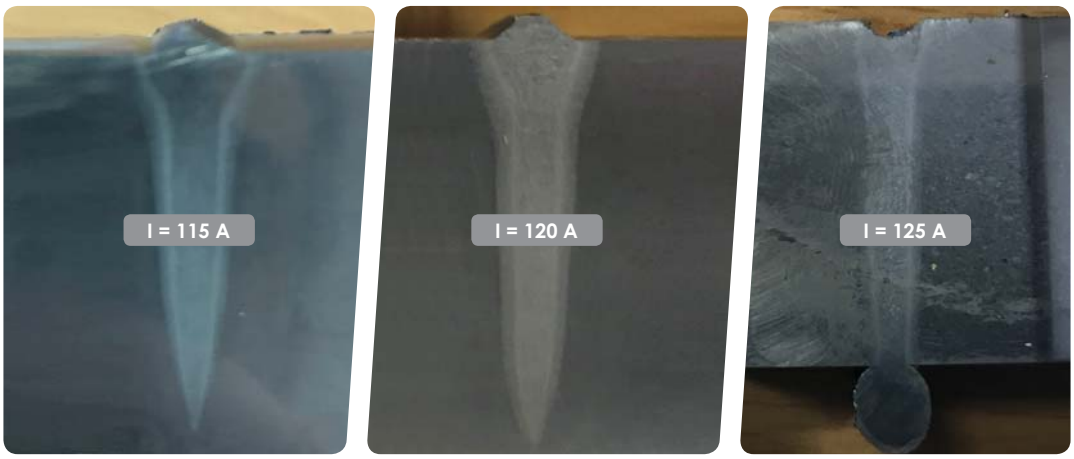

Fig. 5 – 07X12HMБФ-Ш grade pipe sample welded using different beam currents

Subsequently, a pipe with the same seam geometry as the main LPT shaft of the MGT-30 gas turbine was prepared and welded using the selected parameters. Welding parameters are presented in table 5. The optimum welding current in this case was clearly less than that of the weld performed on seamless pipe sample probably due to lower energy levels required for melting and welding under such circumstances.

Table 5 – Welding parameters used for welding of the seamed pipe sample using EBW machine

Rotational speed (deg/min)	Voltage (kV)	Working distance (mm)	Lens current (mA)	Beam current (mA)
273	60	336	400	107

Fig. 6 represents cross-section of the developed seam welded joint. There was no evidence of any defects such as lack of fusion, and the weld seam was properly filled. Post Weld Heat Treatment (PWHT) was also performed for 2 hours at 620 °C to relieve the pipe of any residual stress. Figs. 7(a) and 7(b) show the welded sample following completion of the welding and PWHT processes each.

Fig. 6 – Cross-section of the seam welded joint on 07Х12НМБФ-Ш grade pipe sample

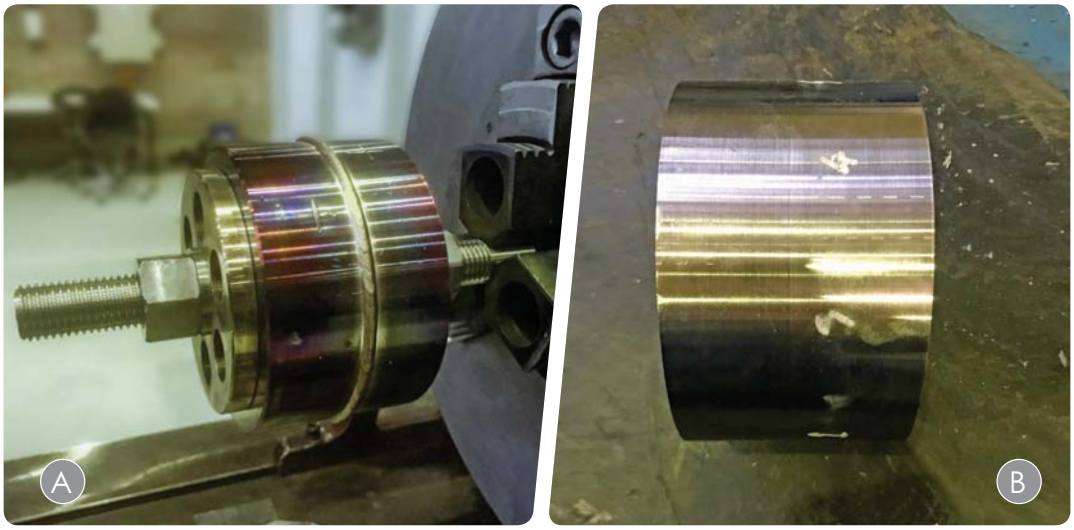

Fig. 7 – Welded seamed pipe sample following completion of the welding (a) and PWHT (b) processes

Welding Test Results

- Mechanical Properties

The results of the tensile and bend tests performed are mentioned in table 6. As it can be seen, the fracture occurs in an area out of the weld zone and the ultimate tensile strength is also more than that of the base material. Regarding the bend test, the results were also acceptable notwithstanding the shorter length of the specimens than that mentioned in the related standard.

Table 6 – Results of the tensile and bend tests carried out on welded pipe specimens

Tensile Test, ISO 15614-11								
Identification	Dimension (mm)	Ultimate (N)	U.T.S (MPa)	Y.S. (MPa)	El. (%)	R.A (%)	Failure Location	Remark
1	5.92×10.96	57456	886	-	-	-	Base	-
2	5.90×11.02	55788	881	-	-	-	Base	-

Bend Test, ISO 15614-11					
Identification	Type	Mandrel Diameter (mm)	Angle of Bend	Result	Remark
1	Side	10	120	Accepted	-
2	Side	10	120	Accepted	-
3	Side	10	120	Accepted	-
4	Side	10	120	Accepted	-

The results of the weld zone Charpy impact test are presented in table 7. The absorbed energy is favorably more than that of the base material and the results are acceptable as well.

Table 7 – Results of the Charpy impact test performed on welded pipe specimen

Specimen No.	Location Notch	Notch Type	Test Temp (°C)	Size (mm)	Lateral Expansion (mm)	Impact Value (J)	Average J
1	WM	V	+23	10 × 10	-	60 56 80	65

■ Microstructural Evaluation

Fig. 8 represents microscopic images of the welded specimen containing weld zone, Heat Affected Zone (HAZ), and base metal. As can be seen from this figure, HAZ area is narrow on either side of the weld zone with fine grain microstructures. The difference between microstructures of the base metal on either side of the joint might be related to different forging conditions such as forging force or forging temperature. Weld metal has also a fine structure resulting from re-melting and re-solidification.

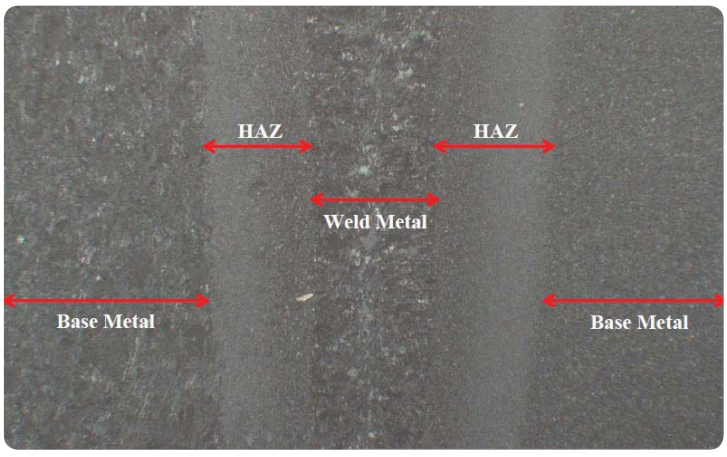

Fig. 8 – Microscopic image of a seamed pipe welded joint specimen representing different weld zones

Fig. 9 shows the microstructure of different zones including base metal, weld metal and HAZ area. The tempered martensitic structure is dominant in all regions. Weld metal contains relatively coarse martensite structures in comparison with the base metal characterized by more equiaxed structures. The reason for such an observation would be melting and rapid re-solidification of the weld metal.

HAZ area is also characterized by fine martensitic structures and the width of these regions is also so narrow due to the nature of EBW and concentration of the heat source in this process. The microstructures of the weld metal and HAZ areas are also different from each other due to re-crystallization that takes place in the HAZ areas, leading to more equiaxed and finer martensitic structures in these regions.

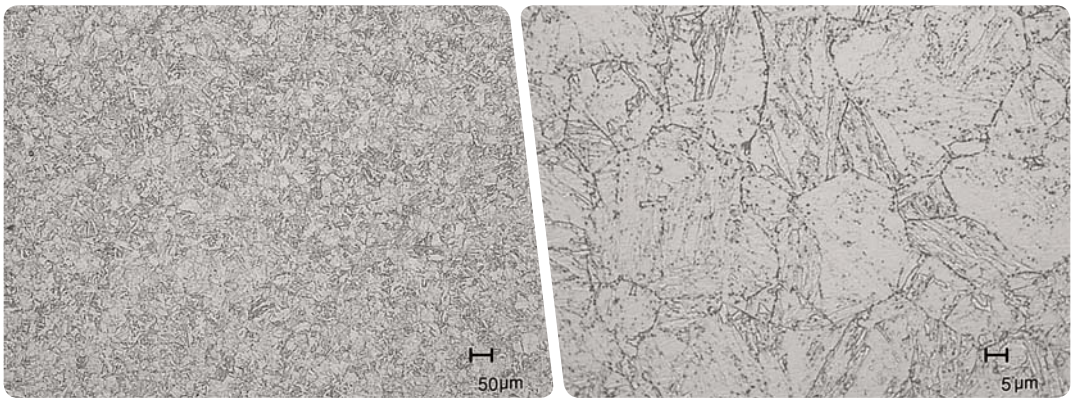

Base Metal

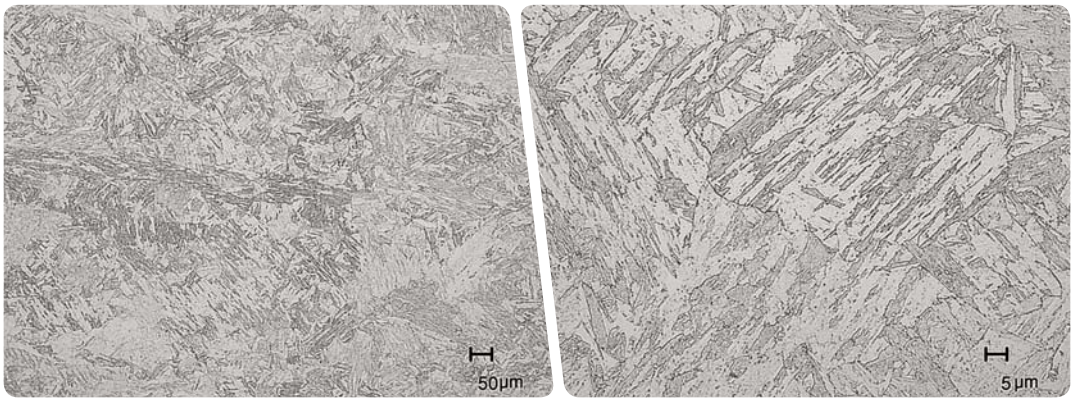

Weld Metal

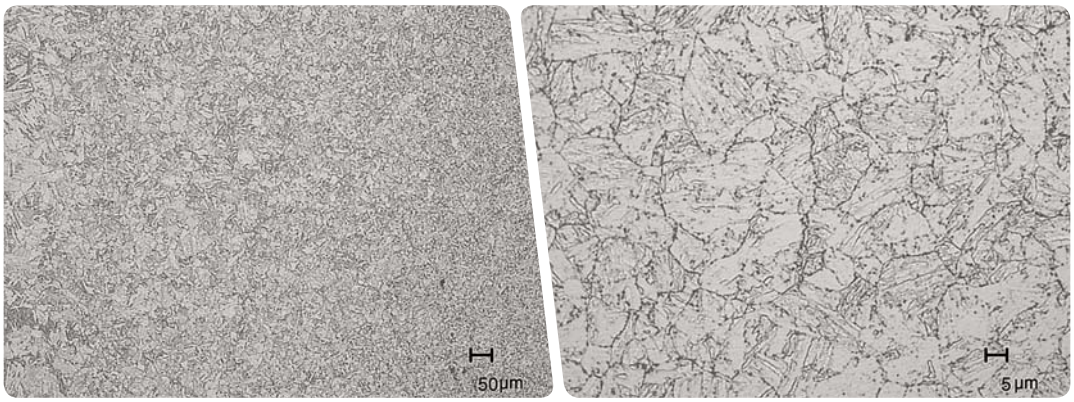

Heat Affected Zone

Fig. 9 – Welded joint microstructures at base metal (top), weld metal (middle), and HAZ area (bottom)

Welding of MGT-30 gas turbine LPT shaft

MGT-30 gas turbine LPT shaft was welded using the ascertained parameters considering a few additional technological requirements, as shown in Fig. 10. The weld seam was visually inspected once the welding was finished. The welded shaft was remained under a tight vacuum of 2.3×10^{-4} mbar for an hour in order to avoid development of any possible defects. The vacuum was then broken but the shaft still remained within the chamber for another hour in order to control its cooling rate. Post weld heat treatment was also performed according to the approved heating cycle to relieve any residual stress.

The results of the radiographic tests were acceptable with no defects detected. The shaft was then sent to go through further machining and finishing operations required prior to assembly.

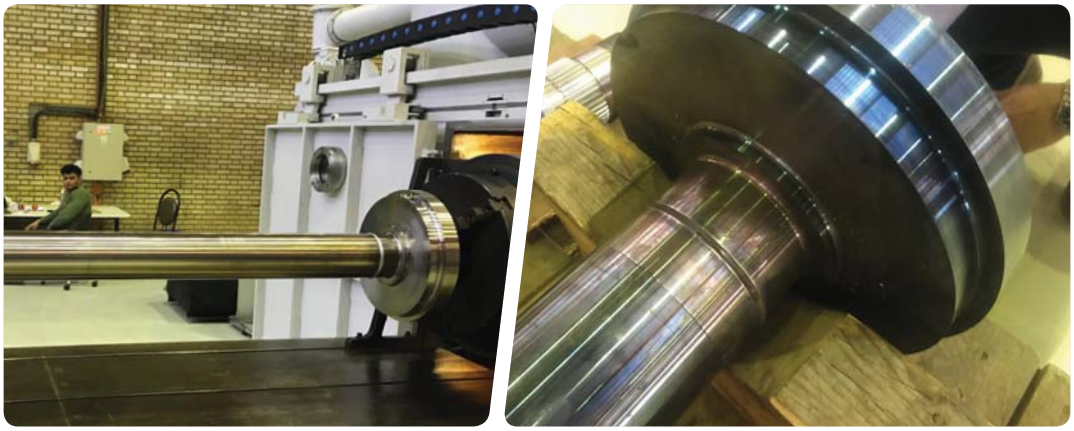

Fig. 10 – Welded LPT shaft of MGT-30 gas turbine

References

[1] John C. Lippold, Damian J. Kotecki (2005); '*Welding Metallurgy and Weldability of Stainless Steels*', John Wiley and Sons, New York, NY, ISBN: 978-0-471-47379-4

[2] Sindo Kou (2003); '*Welding Metallurgy*' (2nd edition), John Wiley and Sons, New York, NY, ISBN: 978-0-471-43491-7

[3] *Recommended Practices for Electron Beam Welding and Allied Processes;* AWS C7.1M/C7.1:2013

5

Development of an Outstanding Coating against Water Droplet Erosion in Gas and Steam Turbine Blades

Introduction

Power output of gas turbines relies on the density of the compressed air. In spite of increasing demand of power and electricity in warm seasons, output power of gas turbines decrease due to the reduction in the density of the inlet air [1]. Wet compression is an attractive solution to enhance gas turbine power and efficiency in hot operational environments given the low capital investment required. However, water droplets from the nebulizer as well as secondary droplets from the condensed water can lead to erosion in the turbine compressor section particularly on the first few stages of rotating blades. Fig. 1 shows a worn out compressor blade of a gas turbine that utilizes wet compression system.

Fig. 1 – Worn compressor blade operating in wet compression system (Courtesy of NCConsulting)

Water droplet erosion also occurs in the blades of low pressure section of a steam turbine. The small primary droplets condensate in bulk of the super-cooled steam in the steam flow, get separated on the blade surface and generate secondary large droplets which are the major cause of the erosion. Especially on large blades in final stages, the high impact energy of the droplets can lead to considerable material loss. It should be noted that, this phenomenon causes huge damage particularly at the leading edges close to the blade tips [2]. The worn area compromises flow characteristics and thus results in reduced power output of the turbine. Fig. 2 depicts an eroded steam turbine blade. Additionally, the individual resonance frequency is changed which could in turn result in high-cycle fatigue (HCF) damage when the blade comes into resonance.

Fig. 2 – Droplet erosion on the leading edge of the last stage blade of a steam turbine (Courtesy of NCConsulting)

The turbine manufacturers have endeavored to find new methods to protect the blades from erosion and its adverse effects.

The fleet operation experience has proven that hard and corrosion resistant materials better withstand water droplet erosion [2,3]. Several surface engineering processes have been performed on LP steam turbine blades and first few stages of gas turbine compressor blades to mitigate water droplet erosion. They include hardening of leading edges (flame/ laser hardening), application of resistant coatings (e.g., thermal spray coatings, PVD coatings, etc.), and shielding the leading edges with specific materials (e.g., Stellite inserts, etc.) [3]. To improve service lifetime of compressor blades and steam turbine blades which are affected by water droplet erosion in MGT-70 gas and MST-50C steam turbines, development of a protective High Velocity Oxy-Fuel (HVOF) sprayed nano-structure coating consisting of tungsten carbide (WC) in cobalt chrome (CoCr) matrix (nano-HVOF WC/CoCr) on blades material was actioned. The tribological properties of the applied coating were investigated using Water Droplet Erosion (WDE) test and its corrosion resistance through salt spray test. Based on the results, nano-WC Co/Cr coating was identified as a proper method to extend blade lifetime in these machines and some other products. This project was accomplished with the collaboration of NCConsulting Company.

Experiments

The WC/ CoCr hardface coating was applied using HVOF spray process consuming nano-powders in accordance with MAPNA Turbine's partner specifications. The utilized WC/CoCr was spherodized by controlled plasma sphero¬dization process to achieve ultra-fine and highly optimized nano-HVOF powder. The spherodized particle makes a matrix consisting of about 14wt% CoCr melted alloy in which sub-micron carbides were metallurgically bonded (Fig. 3). Nano-HVOF WC/CoCr powder presented high deposition efficiency and sprayed surface roughness of around 1 µm. The hardness of coating is more than 1200 HV0.3 with a very was ductility. Since a portion of blade shall be coated with nano-HVOF hardface coating and remaining parts with anti-corrosion coating, Al-pigmented ceramic coating; OT400/100 was applied on corrosion test samples by spraying followed by curing. Al-pigmented ceramic coating performed on gas turbine compressor blades, are intended to protect them against corrosion and to some extent, erosion.

Water droplet erosion tests were performed on coated and bare samples. The utilized WDE test apparatus (Fig. 4) was set to somehow simulate the working conditions of affected blades in gas turbines utilizing wet compression system. The WDE test conditions are mentioned in table. 1.

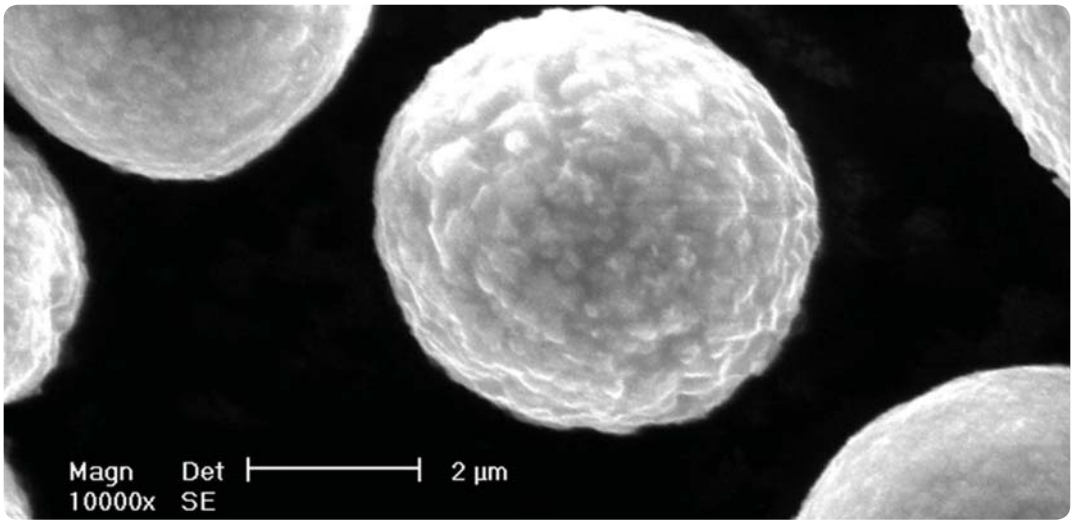

Fig. 3 – Scanning Electron Microscopy (SEM) image of nano-HVOF powder WC/CoCr 86-10-4 (Courtesy of Thermico)

Table 1 - WDE test conditions

Impact speed	400 m/s
Erodent	water (Threefold Distilled H2O)
Impact angle	90°
Testing temperature	RT
Testing pressure	30 mbar

For each run, two samples were tested in the testing chamber. To estimate the eroded volume after each intermediate stop, samples were cleaned using acetone and let them dry up at 70°C for 15 minutes and subsequently weighed the samples using a precision scale. Eroded volume was then calculated.

Fig. 4 – Water droplet erosion test facility (Courtesy of RSE S.p.A)

With an increase in the humidity amount in turbine working atmosphere, the risk of failure due to corrosion fatigue increases. This brought about the idea that coating and bare metal shall be tested using corrosion test methods. It should be noted that frequent fracture of blades due to corrosion pits were reported by Witek [4]. Regarding this, corrosion tests based on the following conditions were performed on the test specimens:

- **Moderate condition:** 1008 hr salt spray test according to ISO 9227:2006/ASTM B117
- **Harsh condition/ wet corrosion:** 1008 hr soaking in saturated NaCl at 60 °C/ pH 7 + 200 hr pH 5

The salt fog spray test was conducted continuously, the test temperature was maintained at 35±2°C and the relative humidity was maintained at 94±4%. Samples were placed in testing chamber at an angle of 15° with the unprotected face upwards. During testing, visual inspections were performed once every 24 hrs. On the basis of microscopic observations and color metallography, the corrosion resistance of samples was then analyzed.

The corrosion tests should simulate the behavior of the hardface coated area adjacent to the intact sacrificial coating (Al-pigmented ceramic coating; OT400/100) to evaluate possible electrochemical interactions like pitting caused by galvanic cell formation between the CoCr matrix and the OT400/100. Therefore the sacrificial coating covering the entire front of the hardface coated specimen was partially removed through precision grinding. In order to simulate harsher corrosion conditions than that in the salt spray test, immersion tests in saturated (+/- 25 %) NaCl at 60 °C were conducted. In the initial test, the pH shall be 7 in maximum. Moreover, test time was 1008 hours like in the salt spray test.

For even more increased corrosivity, the pH value was lowered to pH=5 by addition of some HCl.

The latter test would simulate a severe operational malfunction in a gas turbine installation, e.g., breakdown of air filters for a longer period of operation.

Results and Discussion

The water droplet impacts with high relative velocity cause damage to all materials. Various mechanisms for WDE have been found. The probability of each mechanism occurrence depends on the target material properties and water droplet impact conditions [5]. In general, the water droplet erosion of a material relies on mechanical properties of the material including resilience, hardness, toughness, elastic modulus and tensile strength. Erosion behavior of materials is categorized according to its failure mode: brittle and ductile. Unlike the stainless steel, the erosion resistance of spray coating is roughly related to their fracture toughness [5]. Fig. 5 shows eroded surfaces of coated nano-WC/CoCr sample as well as bare martensitic stainless steel sample.

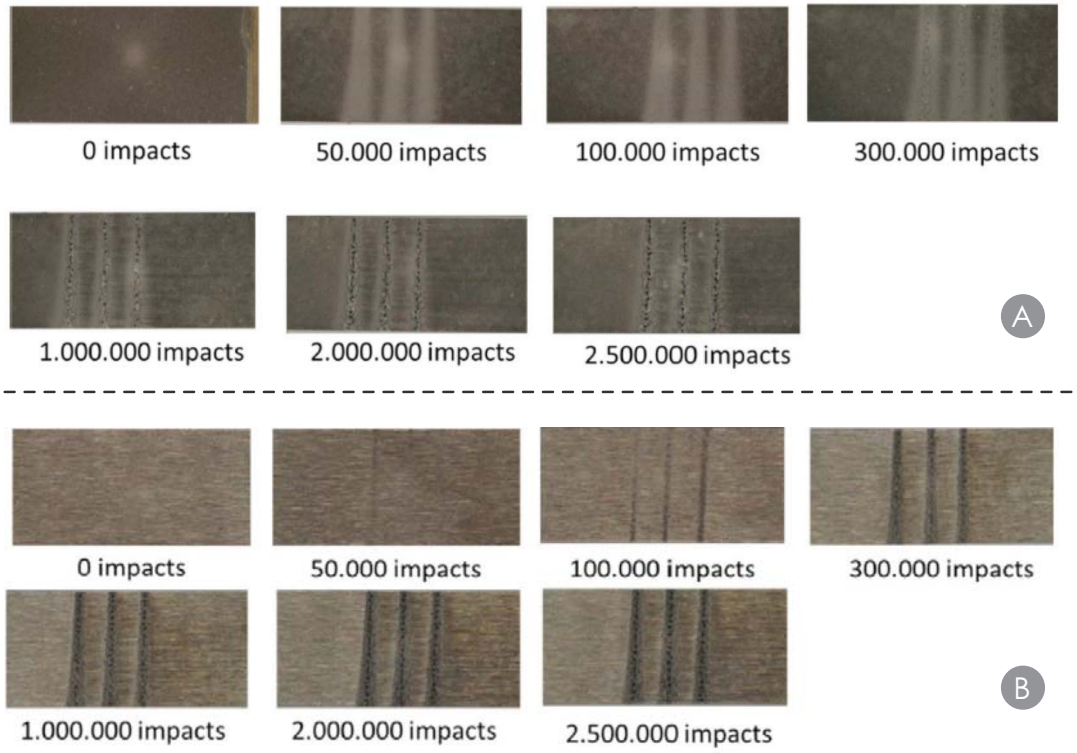

Fig. 5 – Eroded surfaces of nano-WC/CoCr coated sample (A), bare martensitic stainless steel sample (B)

Based on the WDE test results, bare material erosion begins in the commencement of 50,000 water droplet impacts. On the other hand, 300,000 water droplet impacts was identified as the relevant erosion starting point for coated samples. In Fig. 6, graphs of the erosion rates of coated and uncoated samples are shown for 2.5 million water droplet impacts. As shown in this figure, the nano-HVOF WC/CoCr hardface coating was able to protect martensitic stainless steel against the erosion mechanism and increase the lifespan of the blade. Also, there was no coating spallation detected during the water droplet testing due to lack of adhesion and/or cohesion of coating.

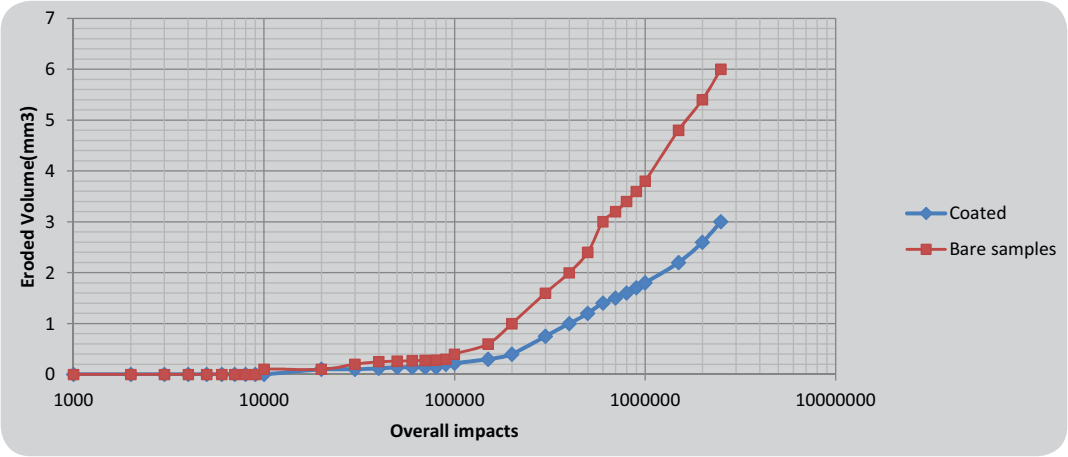

Fig. 6 – Water droplet erosion test results

The salt spray test (fog test) is an accelerated corrosion test used to evaluate the relative corrosion resistance of materials exposed to salt spray or salt fog at ambient and/or slightly elevated temperatures. Test specimens are placed in an enclosed salt spray testing cabinet or chamber and are subjected to a continuous indirect fog or spray of a salt water solution. This is maintained throughout the duration of the test. This simulates accelerated corrosion mechanism in marine or coastal environments.

This test was also carried out for both coated and bare samples according to the guidelines of the ISO 9227:2006/ASTM B117 international standards. Red rust and severe pitting corrosion emerged after 1008 hrs (48 cycles) on the surface of the bare martensitic stainless steel sample. No red rust and pitting was observed on the surface of the coated sample, indicating superior performance of the applied nano-HVOF WC/CoCr coating in an anti-corrosion agent role. The corrosion mechanism of WC/CoCr coated samples is described by Souza et al.: *dissolution of cobalt and tungsten subsequent to anodic polarization of cemented carbides* [6].

Fig. 7 shows surfaces of the coated and bare samples prior and after the corrosion test. Furthermore, results of wet corrosion tests performed in PH=7 and PH=5 confirmed outstanding anti-corrosion behavior of the coating applied in both normal and harsh operating conditions.

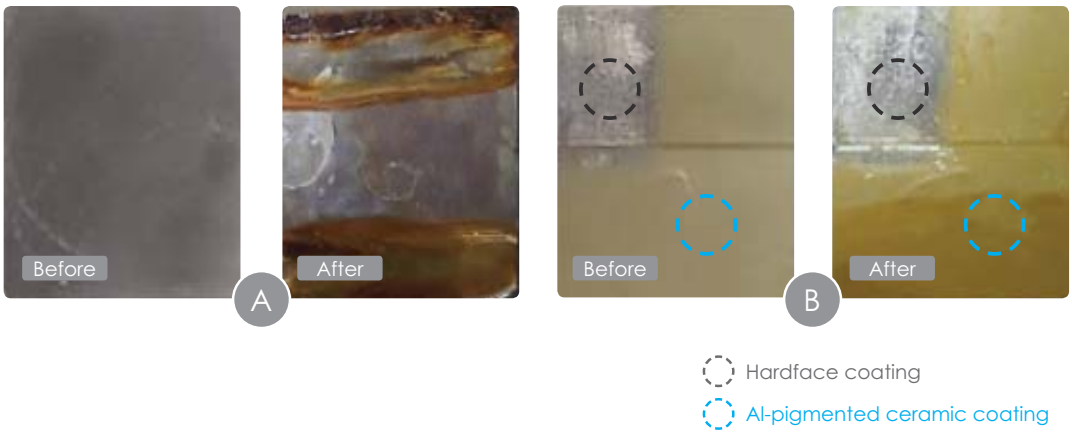

Fig. 7 – Bare (A) and coated (B) samples prior and after implementation of corrosion tests

Conclusion

In order to increase the lifetime of turbine components e.g. gas turbine compressor and LP steam turbine blades with compression system and water droplets erosive conditions, a new hardface coating was developed and an evaluating test program was specified. Water droplet erosion test proved better performance of the coating over longer test periods with lower erosion rates compared to base material. Also, adhesion of hardface coating was not affected by stresses occurring in the test. The result of the relatively salty shower corrosion test (1008 hr) can be considered as "Passed" according to ASTM evaluation rules. Also coating system didn't fail under harsh and medium corrosion tests. Consequently, the proposed nano-HVOF WC/CoCr hardface coating is a proper and reliable method to be applied on first few stages of gas turbine compressor and steam turbine blades in wet compression system and final low pressure stages, respectively.

References

[1] Dharmadhikari, S. and Andrepont, J.S., 'Boost Gas Turbine Performance by Inlet Air Cooling', Hydrocarbon Processing, February 2004, 77-84

[2] B.S. Mann, Vivek Arya, 'HVOF Coating and Surface Treatment for Enhancing Droplet Erosion Resistance of Steam Turbine Blades', Wear, Vol. 254(2003), 652-667

[3] Joerg Schuerhoff, Andrei Ghicov, Karsten Sattler, 'Advanced Water Droplet Erosion Protection for Modern Low Pressure Steam Turbine Steel Blades', ASME GT2015-43140, ASME Turbo Expo 2015, Montreal, Quebec, Canada

[4] Lucjan Witek, 'Crack Propagation Analysis of Mechanically Damaged Compressor Blades Subjected To High Cycle Fatigue', Engineering Failure Analysis, Vol. 18(2011), 1223-1232

[5] M.S. Mahdipoor, F. Tarasi, C. Moreau, A. Dolatabadi, M. Medraj, 'HVOF Sprayed Coatings of Nano-Agglomerated Tungsten-Carbide/Cobalt Powders for Water Droplet Erosion Application', Wear, Vol. 330-331(2015), 338-347

[6] V. A. D. Souza, A. Neville, 'Mechanisms and Kinetics of WC-CO−CR High Velocity Oxy-Fuel Thermal Spray Coating Degradation in Corrosive Environments', Journal of Thermal Spray Technology, Vol. 15(2006), 106-117

Head Office:
231 Mirdamad Ave. Tehran, I.R.Iran.
P.O.Box: 15875-5643
Tel: +98 (21) 22908581
Fax: +98 (21) 22908654

Factory:
Mapna blvd., Fardis, Karaj, I.R.Iran.
Post code: 31676-43594
Tel: +98 (26) 36630010
Fax: +98 (26) 36612734

www.mapnaturbine.com
tr@mapnaturbine.com

GR260-0